Nano Research

ISSN 1998-0124 CN 11-5974/O4
https://doi.org/10.1007/s12274-024-6899-4

Research Article

Nanoshell-driven carrier engineering of large quantum dots enables ultra-stable and efficient LEDs

Dandan Zhang[§], Jianshun Li[§], Lei Wang (✉), Yaqi Guo, Weipeng Liu, Qingli Lin, Lin Song Li, and Huaibin Shen (✉)

Key Laboratory for Special Functional Materials of Ministry of Education, National and Local Joint Engineering Research Center for High-efficiency Display and Lighting Technology, Henan University, Kaifeng 475004, China
[§] *Dandan Zhang and Jianshun Li contributed equally to this work.*

Received: 24 May 2024 / **Revised:** 4 July 2024 / **Accepted:** 18 July 2024

ABSTRACT

Quantum dot (QD) light-emitting diodes (QLEDs) have been considered one of the most promising candidates for next-generation lighting and displays. However, the suboptimal carrier dynamics at the interface between QDs and the hole transport layer (HTL), such as leakage and quenching induced by the accumulation of electrons at high brightness, severely deteriorates the device's efficiency and stability. Here, we introduced the influence of carrier modulation by nanoshell engineering on the external quantum efficiency (EQE) and operation lifetime for QLEDs with large-sized QDs. The shell-driven engineering of energy level positions and band bending effectively eliminates the hole injection barrier and promotes charge injection balance. Photo-assisted Kelvin probe technique reveals that the ZnCdSe/ZnSeS QD/TFB (TFB = poly(9,9-dioctylfluorene-co-N-(4-(3-methylpropyl))diphenylamine)) interface presents an increased surface potential and quasi-Fermi level splitting, reducing heat generation during device operation at high brightness. The shell-driven carrier engineering strategy reveals that our devices exhibit a high external quantum efficiency of 26.44% and an ultralong operation time (exceeding 50,000 h) to 95% of the initial luminance at 1000 cd/m^2 (T_{95}@1000 cd/m^2). We anticipate that our results provide insights into resolving the issues at the QD-HTL interface and demonstrate the importance of carrier management driven by QD nanostructure tailoring for the commercialization of QLEDs.

KEYWORDS

large-sized quantum dots, shell-driven carrier engineering, band bending, ultra-stable operation lifetime

1 Introduction

Solution-processed quantum dots (QDs) are promising candidate materials for the next generation of display and lighting technologies due to their low cost and outstanding optoelectronic properties [1–5]. Highly efficient quantum dot light-emitting diodes (QLEDs) continue to emerge, accompanied by increasing operational lifetimes, especially T_{95}@1000 cd/m^2 (the time for the initial luminescence of 1000 cd/m^2 decreases to 95%) [6–8]. Recently, large-sized QDs (diameter > 15 nm) have shown great potential in QLEDs due to suppressed Förster resonance energy transfer (FRET), nonradiative Auger recombination, and higher exciton formation probability [9–13]. For example, QLEDs based on large-sized CdSe core/shell QDs can achieve quasi-Fermi level splitting enhancement and heat generation minimization, resulting in high power conversion efficiency and excellent T_{95} operation lifetime [10]. How to effectively manage the carrier dynamics in large-sized QLEDs is an urgent issue in promoting the commercialization of QLEDs.

Currently, efficient QLEDs usually adopt an organic–inorganic hybrid device structure, in which solution-processed poly(9,9-dioctylfluorene-co-N-(4-(3-methylpropyl))diphenylamine) (TFB) and zinc-based oxide are used as hole transport layer (HTL) and electron transport layer (ETL), respectively [3, 6, 14, 15]. Various strategies, such as introducing interlayers and adjusting the energy level positions of ETL or HTLs, are used to promote balanced charge injection [16–24]. However, due to the intrinsic structural differences between organic polymers and oxide semiconductors, as well as the significant difference in injection barriers between them and QDs, the imbalance in electron and hole injection remains a major reason limiting the device efficiency and stability. The unbalanced carrier injection leads to an excess accumulation of electrons at the QD layer and QD/TFB interface [8, 25–27]. Taking into account the energetic disorder of TFB, excess electrons accumulated at the interface would still leak into the HTL layer or undergo quenching, which leads to the decomposition of TFB [15, 22, 28, 29]. This is currently a main factor limiting the enhancement of external quantum efficiency (EQE) and the rapid deterioration of operational lifetime at high brightness. Recently, we introduced a unique strategy to reduce the packing number in the emitting layer by using large QDs, which increases the charge population per QD, thereby minimizing device heating [10]. This motivates us to design unique QD nanostructures to further carrier engineering, thereby elucidating their intrinsic relationship with device efficiency and T_{95} lifetime.

Here, we demonstrate ultra-stable and highly efficient QLEDs by shell-driven carrier engineering. We elucidate the influence of shell composition on EQE and T_{95}@1000 cd/m^2 lifetime by synthesizing novel QDs with giant-sized cores and different

Address correspondence to Lei Wang, wanglei7869@henu.edu.cn; Huaibin Shen, shenhuaibin@henu.edu.cn

composition shells. The synthesized ZnCdSe QDs with alloy ZnSeS shell not only exhibit the balanced carrier injection but also increase the surface potential and quasi-Fermi level splitting, which are proved by ultraviolet photoelectron spectroscopy (UPS) and photo-assisted Kelvin probe technologies. Further precisely controlled shell growth can significantly promote the band bending and heat generation minimum, achieving an EQE greater than 26% and a T_{95}@1000 cd/m^2 lifetime exceeding 50,000 h. Our results provide insights into addressing the stability of blue QLEDs and lay the groundwork for the development of QLED printing technology.

2 Results and discussion

Three types of QDs with large alloyed ZnCdSe cores and different shell compositions were synthesized through a one-pot two-step method (Fig. S1 in the Electronic Supplementary Material (ESM)). Firstly, selenium precursor was injected into the mixed precursors of Cd and Zn, and large ZnCdSe QDs were generated as cores. When selenium precursor was injected into the system for 5 min, the photoluminescence (PL) peak of ZnCdSe cores was located at 615 nm (Fig. S2(a) in the ESM). As the reaction time increased to 30 min, the PL peak gradually red-shifted, accompanied by a gradual narrowing of full width at half maximum (FWHM). Subsequently, the PL peak remained almost unchanged. The synthesized ZnCdSe cores show a PL emission peak of 645 nm with a 23 nm of FWHM. These samples present an average particle size of 12.28 ± 1.65 nm and a wurtzite crystal structure (Fig. S3 in the ESM). Subsequently, three zinc-chalcogenide precursors (ZnSe, ZnSeS, and ZnS) were injected for shell growth. Finally, ZnCdSe/ZnSe, ZnCdSe/ZnSeS, and ZnCdSe/ZnS QDs with 5 monolayers (ML) were successfully synthesized. As the ZnSeS shell further grows, the PL peak of QDs gradually blue-shifts from 645 to 640 nm, which indicates the alloy formation due to the high-temperature shell growth process (Fig. S2(b) in the ESM). The synthesized QDs with three distinct shells exhibit a narrow FWHM of 22 nm at the emission peaks near 640 nm, as shown in Fig. 1(a). The average sizes of ZnCdSe/ZnSe, ZnCdSe/ZnSeS, and ZnCdSe/ZnS samples increase from 12.28 ± 1.65 nm of ZnCdSe cores to 15.42 ± 1.15, 15.49 ± 1.00, and 15.27 ± 1.00 nm, respectively (Fig. 1(b)). Additionally, it can be observed that three kinds of QDs have a close-to-spherical morphology and exhibit good monodispersity and size uniformity from transmission electron microscopy (TEM) images. X-ray diffraction (XRD) was employed to explore the impact of three kinds of shells on the ZnCdSe crystal structure. All three samples reveal the (100), (002), and (101) crystal facets in the wurtzite crystal structure, verifying that all three shell materials do not disrupt the lattice structure of ZnCdSe cores [6]. Importantly, these core/shell QDs reveal a gradual evolution of the (100) and (002) crystal planes compared to ZnCdSe cores. With the growth of the shell layer, the proportion of the (002) facet significantly increases. As shown in Fig. S4 in the ESM, the intensity ratio values of the (002) to (100) facets in QDs with ZnS, ZnSeS, and ZnSe shells are 0.95, 1.01, and 1.15, respectively. We believe that the reason for the crystal facet evolution is due to the differences in the precursor reactivity of three shell materials, as well as the varying lattice match with ZnCdSe cores, which usually affects the energy level positions and quantum yield (QY) of QDs. UPS technique was used to analyze the energy levels in QDs. Due to the large core size (> 12 nm), three types of core/shell QDs have the same Fermi level. In comparison to the valence band maximum (VBM) of ZnCdSe/ZnS QDs at −6.05 eV, ZnCdSe/ZnSe and ZnCdSe/ZnSeS QDs exhibit higher VBM of −5.61 and −5.71 eV, respectively. The significant upward shift in VBM usually indicates that LEDs based on ZnCdSe/ZnSe and ZnCdSe/ZnSeS QDs have a reduced hole injection barrier. The QYs of the synthesized core/shell QDs with ZnSe, ZnSeS, and ZnS shells are 91%, 94%, and 90%, respectively. Compared to the QY exceeding 90% of all QD solutions, the QYs of all QD films only show a slight decrease, all exceeding 80%, demonstrating excellent FRET suppression (Fig. S5 in the ESM). Among them, ZnCdSe/ZnSeS films exhibit the highest QY of 86%.

With these different shells QDs, three kinds of QLEDs were built by the typical multilayered organic–inorganic hybrid architecture, as shown in Fig. 2(a). A monolayer of large quantum dots was observed from the cross-sectional TEM image. Taking into account the charge injection balance caused by higher VBM, QLEDs based on ZnCdSe/ZnSe and ZnCdSe/ZnSeS QDs exhibit lower leakage current and turn-on voltage ($V_{\text{turn-on}}$, voltage at a luminance (L) of 1 cd/m^2, Fig. 2(b)). As the voltage increases, the electroluminescence (EL) peak positions of the three types of devices do not show an obvious shift, exhibiting excellent color stability (Fig. S6 in the ESM). We extracted EQE–voltage curves of QLEDs using monolayers of QDs with different shells (Fig. S7 in the ESM). The driving voltages of the maximum EQE for devices using QDs with ZnSe, ZnSeS, and ZnS shells are ~ at 2.36, 2.36, and 2.73 V, respectively, although all three devices exhibit relatively low operating voltages, approximately 1.22–1.41 times the bandgap voltage (1.94 V). Consequently, devices based on ZnCdSe/ZnSeS QDs exhibit the highest maximum EQE of 25.09% and peak current efficiency (CE) of 27.2 cd/A at a brightness of 4320 cd/m^2 (Fig. 2(c)). Meanwhile, the maximum EQE of devices based on ZnCdSe/ZnSe and ZnCdSe/ZnS is 23.9% and 22.49%

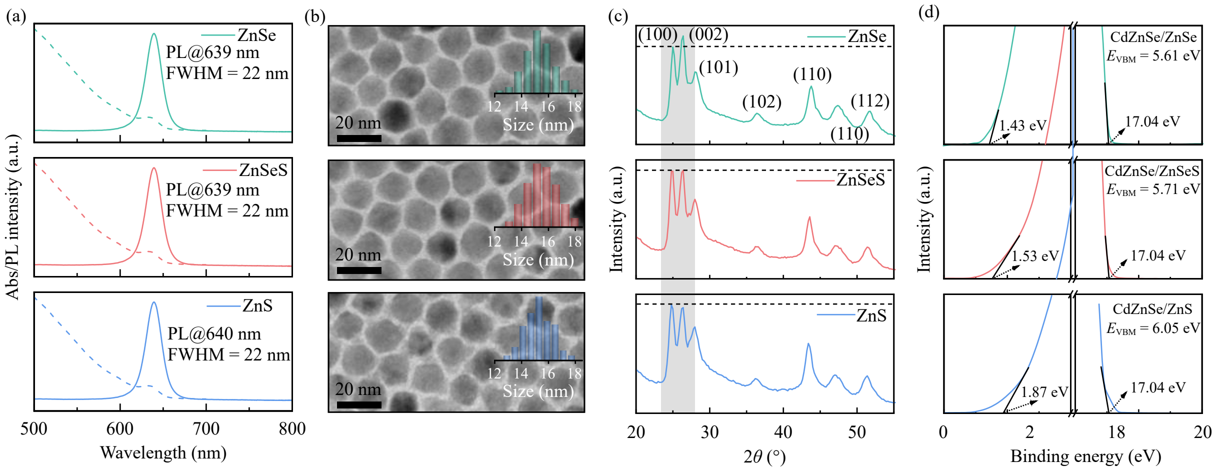

Figure 1 (a) Absorption and PL spectra. (b) TEM images. The insets: size distributions. (c) XRD patterns. (d) UPS spectra for ZnCdSe/ZnSe, ZnCdSe/ZnSeS, and ZnCdSe/ZnS QDs.

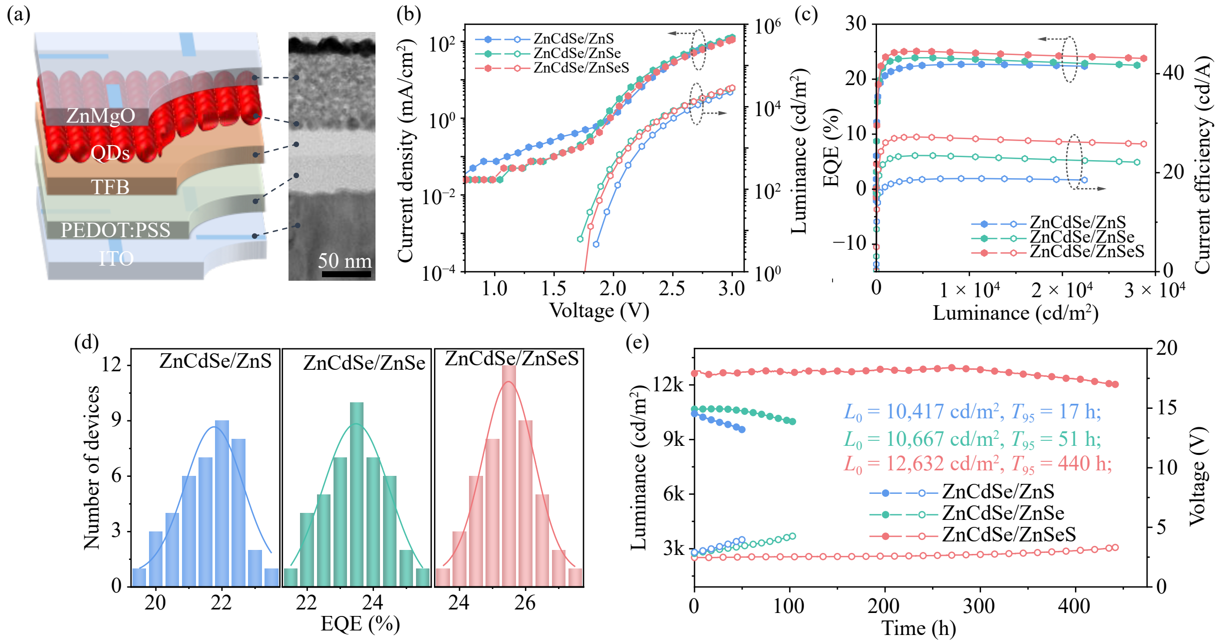

Figure 2 (a) Typical device architecture (left) and cross-sectional TEM image (right) for QLEDs. (b) *J*–*L*–*V* curves. (c) EQE–*L*–CE curves. (d) Histograms of maximum EQEs. (e) *L*–time–*V* curves for QLEDs with ZnCdSe/ZnSe, ZnCdSe/ZnSeS, and ZnCdSe/ZnS QDs.

respectively. We conducted statistical analysis on the EQE of 30 devices based on three types of QD-based LEDs in Fig. 2(d), indicating that it was consistent with the above results and had good reproducibility.

To investigate the influence of three types of QDs on the operational stability of the devices, we tested the T_{95} operational lifetimes (time taken for the brightness to decay to 95% of the initial brightness) of three types of QLEDs under conditions of 30%–40% relative humidity and a temperature of 20–23 °C. The operational lifetime results were obtained under a constant current density (*J*). As shown in Fig. 2(e), the ZnCdSe/ZnS-QLED, ZnCdSe/ZnSe-QLED, and ZnCdSe/ZnSeS-QLED devices, with initial brightness (L_0) of 10,417, 10,667, and 12,632 cd/m², exhibited T_{95} lifetimes of 17, 51, and 440 h, respectively. We further extracted the acceleration factor (*n*) based on the empirical equation $(L_0)^n \times T_{95}$ = constant through testing the T_{95} lifetime at different brightness (Fig. S8 in the ESM). The values of *n* for devices with ZnCdSe/ZnS, ZnCdSe/ZnSe, and ZnCdSe/ZnSeS QDs are 1.85, 1.83, and 1.82, respectively. Then, The T_{95} lifetimes at an initial brightness of 1000 cd/m² are estimated to be 1294 and 3880 h, respectively. What is remarkable is that the estimated T_{95} value for the ZnCdSe/ZnSeS-based QLEDs reaches 44,476 h.

We systematically explored the carrier dynamics processes in three types of QLEDs to deeply explore the influence of shell composition on the EQE and operational lifetime of devices. The energy level diagram of three kinds of QDs was extracted from UPS and ultraviolet–visible (UV–vis) absorption spectra results. The CBM and VBM values of TFB are −2.2 and −5.3 eV, respectively, which are derived from our previous literature [30]. For ZnCdSe/ZnSeS and ZnCdSe/ZnSe QDs, the VBM energy differences (Δ*E*) between QDs and TFB are 0.41 and 0.31 eV, respectively, which are less than that of 0.75 eV between ZnCdSe/ZnS QDs and TFB (Fig. 3(a)). The significantly reduced Δ*E* implies a smoother hole injection process in ZnCdSe/ZnSeS and ZnCdSe/ZnSe QD-devices. The unbalanced charge injection could lead to the accumulation of excess electrons in the QD layer

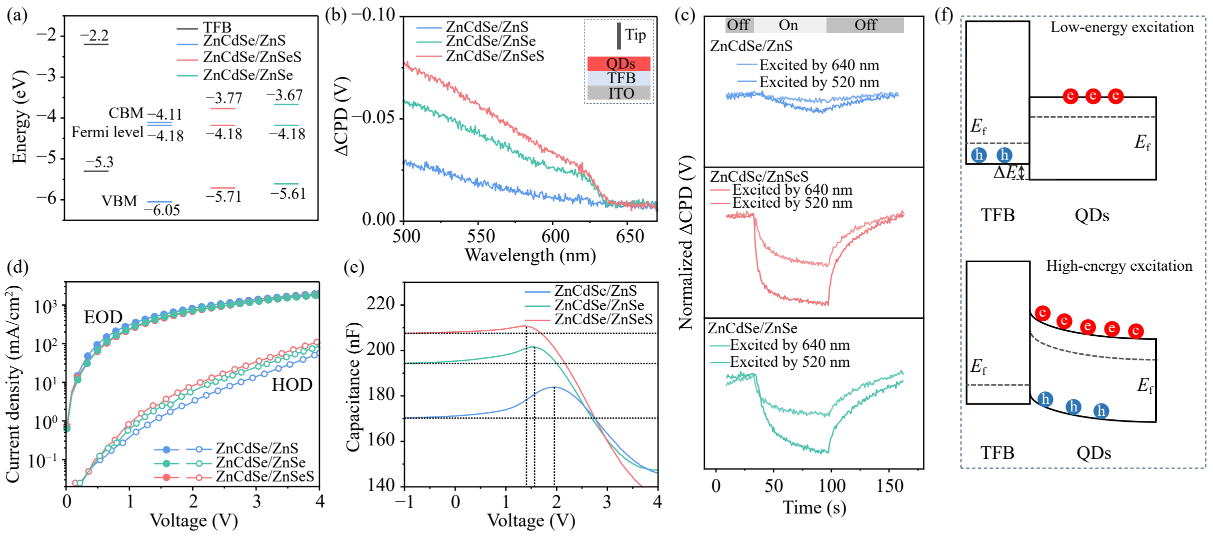

Figure 3 (a) Energy level diagram of TFB and three kinds of QDs. (b) Surface photovoltage spectra. The inset is a schematic of sample measurement. (c) SPV evolution using excitation at 640 and 520 nm. The bars at the top represent the on-off status of the excitation light. (d) *J*–*V* curves of EOD with ITO/ZnMgO/QDs/ZnMgO/Al, and HOD with ITO/PEDOT:PSS/TFB/QDs/MoO$_3$/Al. (e) Capacitance–voltage curves. (f) Energy band diagrams of TFB/QDs interface under different illumination (top: low-energy excitation, and bottom: high-energy excitation), including the band structure and charge distribution.

and the QD/TFB interface, which would increase the possibility of non-radiative recombination and lead to the degradation of TFB [19, 22, 26]. This results in a decrease in device efficiency and a deterioration of the operational lifetime. The photo-assisted Kelvin probe technique achieves non-contact acquisition of work function difference by testing the contact potential difference (CPD) between the tip and the sample [31–34]. The change of CPD (ΔCPD) with the excitation light, called surface photovoltage, indicates the change in surface band bending. We tested the surface photovoltage spectra of ZnCdSe QDs with different shells using a structure of ITO/TFB/QD (ITO = indium tin oxide, Fig. 3(b)). The three samples exhibit significantly different CPD responses, and the corresponding differences become more pronounced as the excitation light wavelength decreases. The evolution of the ΔCPD value is attributed to the change in charge concentration in the space-charge region, so it gives information about the change in charge population. The ΔCPD values of ZnCdSe/ZnS, ZnCdSe/ZnSe, and ZnCdSe/ZnSeS QDs under an excitation light at 640 nm are −0.0072, −0.0092, and −0.0102 V, respectively. Using high-energy excitation light at 520 nm, the corresponding values of the three samples increase significantly to −0.0267, −0.0538, and −0.0861 V, respectively. The increasing difference in negative values implies an upward band bending and increased electron population [33]. The higher electron concentration was the intrinsic origin of the increased surface potential and quasi-Fermi level splitting in the ZnSeS shell [10]. At the beginning of illumination, the ZnCdSe/ZnSeS QD sample exhibits a faster and stronger signal response compared to the other two samples, especially under high-energy excitation light (520 nm, Fig. 3(c) and Fig. S9 in the ESM). The significant differences in the response intensity and response speed for large-sized QDs with different shells imply distinct band bending, electron concentration, and quasi-Fermi level splitting, which affect the efficiency and operational lifespan of QD-based devices. In the quasi-thermal equilibrium state by optical excitation or bias voltage, the carrier concentration in QDs will change, thereby affecting the position of the Fermi level and the band bending. Therefore, the difference in band bending from the surface photovoltage measurements gradually increases, due to different charge populations for three kinds of QDs, especially at high excitation energies. This result indicates that the ZnCdSe/ZnSeS QD/TFB interface has an increased surface potential and quasi-Fermi level splitting, which is conducive to reducing heat generation during the device operation state. In addition, we further built electron-only devices (EOD: ITO/ZnMgO/QDs/ZnMgO/Al) and hole-only devices (HOD: ITO/PEDOT:PSS/TFB/QDs/MoO_3/Al, PEDOT:PSS = poly(3,4-ethylenedioxythiophene):polystyrenesulfonate) in Fig. 3(d). The larger current density of the HOD device with ZnCdSe/ZnSeS implies accelerated hole injection, effectively promoting the balance of charge injection. The capacitance (*C*)–voltage measurement is used to monitor the carrier dynamics process under bias voltage. The *C* values of three types of QLED devices show a slow and slight increase within the voltage range of 0–1 V. Subsequently, as the voltage increases, the *C* values begin to increase rapidly, indicating the drastic charge injection process accompanied by charge accumulation at the QD and QD/FTB interface. The peak *C* values of devices with ZnCdSe/ZnSeS measured at lower voltages further confirm their more balanced charge injection compared to ZnCdSe/ZnSe and ZnCdSe/ZnS QLEDs. Although the Δ*E* between ZnCdSe/ZnSeS QDs and TFB is greater than that of the ZnCdSe/ZnSeS QDs/TFB interface, the ZnCdSe/ZnSeS-based QLEDs reveal a more balanced charge injection. We believe that under external excitation, large ZnCdSe/ZnSeS QDs reveal an upward band bending and increased electron population, leading to a weakening of the hole injection barrier.

To investigate the influence of the upward band bending under high-energy excitation on the heat generation of QLEDs, we recorded the changes in the surface temperature of QLEDs under high excitation energy by infrared (IR) thermography (Fig. 4). At

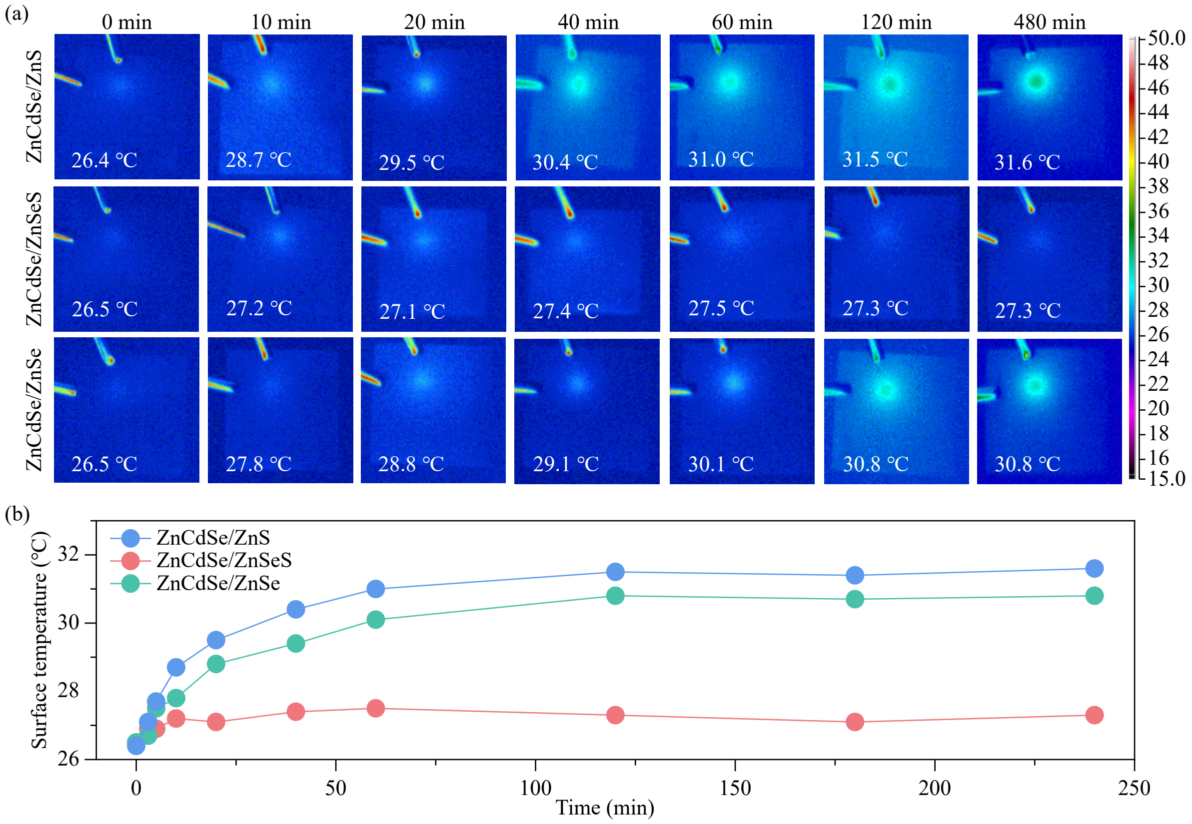

Figure 4 Heat generation of three types of QLEDs at the brightness of 20,000 cd/m². (a) IR images of QLEDs. (b) Surface temperature evolution with the operation time.

the brightness of 20,000 cd/m^2, the device temperature of devices with ZnCdSe/ZnS and ZnCdSe/ZnS QDs rises rapidly. For ZnCdSe/ZnS-based QLEDs, the device temperature increases from 26.4 to 31.0 °C after 60 min of operation. During this period, the device temperature also increases by 3.6 °C in LEDs with ZnCdSe/ZnSe QDs. On the contrary, the surface temperature of ZnCdSe/ZnSeS-based devices increases by only 1.0 °C and does not show any further increase within the next 3 h. Therefore, the shell composition-induced crystal facet evolution can adjust the energy level positions of QDs, reducing the hole injection barrier and promoting the carrier injection balance. In addition, it leads to an increased surface potential and quasi-Fermi level splitting, which is conducive to reducing heat generation during the device operation state [10, 29]. Based on these, QLEDs based on ZnCdSe/ZnSeS QDs exhibit the highest maximum EQE of 25.09% and a T_{95}@1000 cd/m^2 of 44,476 h, which is superior to devices with CdZnSe/ZnSe and CdZnSe/ZnS QDs.

To further verify the influence of nano-shell engineering on the performance of large-sized ZnCdSe-based QLEDs, we further fine-tuned the shell thickness of ZnCdSe/ZnSeS and fabricated QLED devices. The synthesized ZnCdSe-based core/shell QDs with 4, 4.5, 5, and 5.5 ML ZnSeS shells exhibit nearly identical absorption and PL spectra, with PL peaks at 639 nm and FWHM of 22 nm (Fig. 5(a)). All samples show good monodispersity, with the average particle size of QDs increasing from 14.86 ± 0.79 to 15.80 ± 0.50 nm as the ZnSeS shell thickness increases from 4 to 5.5 ML (Fig. 5(b)). Crystal facet evolution by ZnSeS shell thickness is monitored through XRD shown in Figs. S10 and S11 in the ESM. The intensity ratio values of the (002) to (100) facets in QDs with 4, 4.5, 5, and 5.5 ML ZnSeS shells are 0.88, 0.93, 1.01, and 1.03, respectively. UPS test results show that fine-tuning shell thickness has almost no significant impact on the energy level positions of QDs (Fig. 5(c) and Fig. S12 in the ESM). Surface photovoltage spectra indicate that the values of CPD are nearly identical at low excitation energy while showing significant differences at high excitation energy (Fig. 5(d)). The corresponding ΔCPD values of ZnCdSe QDs with 4, 4.5, 5, and 5.5 ML ZnSeS decrease significantly to −0.0754, −0.0947, −0.0861, and −0.0806 V, respectively. The differences in response values imply that the four types of large-sized ZnCdSe-based QDs have varying degrees of upward band bending. Furthermore, surface photovoltage evolution under the on-off switch of the excitation light demonstrates that all four samples exhibit stable response signals after four cyclic tests (Fig. 5(e)). In comparison to the other samples, ZnCdSe/4.5 ML ZnSeS QDs reveal a faster signal response. These results of photo-assisted Kelvin probe measurements indicate that fine-tuning the shell thickness of large-sized QDs can further adjust the extent of band bending upward, promoting hole injection and quasi-Fermi level splitting.

Due to their similar sizes, QYs, and energy level positions, the four types of QLEDs exhibit analogous *J*–*V*–*L* curves (Fig. S13 in the ESM). As the shell thickness increases from 4 to 5.5 ML, the maximum EQEs of ZnCdSe QD-based devices with 4, 4.5, 5, and 5.5 ML ZnSeS shells are 25.99%, 26.44%, 25.86%, and 23.54%, with corresponding *L* values of 10,960, 13,690, 19,600, and 16,380 cd/m^2, respectively (Fig. 6(a)). All four types of QLED devices exhibit low $V_{\text{turn-on}}$, with the device with ZnCdSe/4.5 ML ZnSeS having a $V_{\text{turn-on}}$ of 1.55 V, which is only 80% of its bandgap (Fig. 6(b)). No peak shift is observed in the EL spectra of QLEDs based on ZnCdSe/4.5 ML ZnSeS when the voltage increases from 2 to 4 V (Fig. S14 in the ESM). This usually means that there is no observable quantum-confined Stark effect and serious heat generation during the operation of the device. Crucially, fine-tuning the shell thickness has a significant impact on the T_{95} lifetime of the devices. We tested the T_{95} lifetimes of the four types of QLEDs under an initial brightness greater than 10,000 cd/m^2 (Fig. 6(c)). The corresponding *n* values are 1.81, 1.81, 1.82, and 1.83, respectively (Fig. S15 in the ESM). For comparison, the estimated T_{95} lifetime values at the brightness of 10,000 cd/m^2 are 475, 790, 632, and 511 h, respectively. The statistical results of the T_{95} lifetime values at the brightness of 10,000 cd/m^2 for multiple devices demonstrate good repeatability (Fig. 6(d)). For the optimal ZnCdSe/4.5 ML ZnSeS QD device, the estimated T_{95} lifetime at the brightness of 1000 cd/m^2 is 50,975 h, which is currently the highest recorded value for QLED, as far as our knowledge [4, 7, 10, 15, 22, 35, 36]. Nanoshell tailoring of larger QDs can adjust the energy level position and band bending, eliminate the hole injection barrier, and further promote radiative recombination. Meanwhile, fine-tuning the composition and thickness of the shell layer contributes to increasing the surface potential and the quasi-Fermi level splitting, thereby reducing device heat generation.

3 Conclusions

In summary, we systematically explored the effect of nanoshell tailing of large QDs on carrier modulation of the QD–HTL

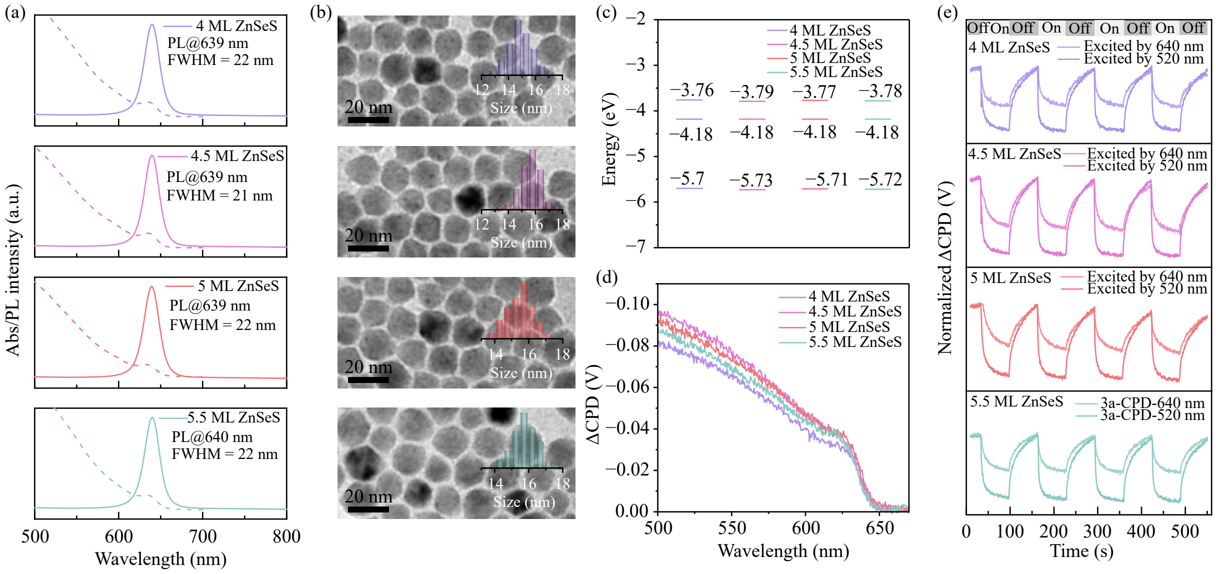

Figure 5 (a) Absorption and PL spectra. (b) TEM images. The insets: size distributions. (c) Energy level diagram of TFB and ZnCdSe QDs with 4, 4.5, 5, and 5.5 ML ZnSeS shells. (d) Surface photovoltage spectra. (e) Surface photovoltage evolution using excitation at 640 and 520 nm. The bars at the top represent the on-off status of the excitation light.

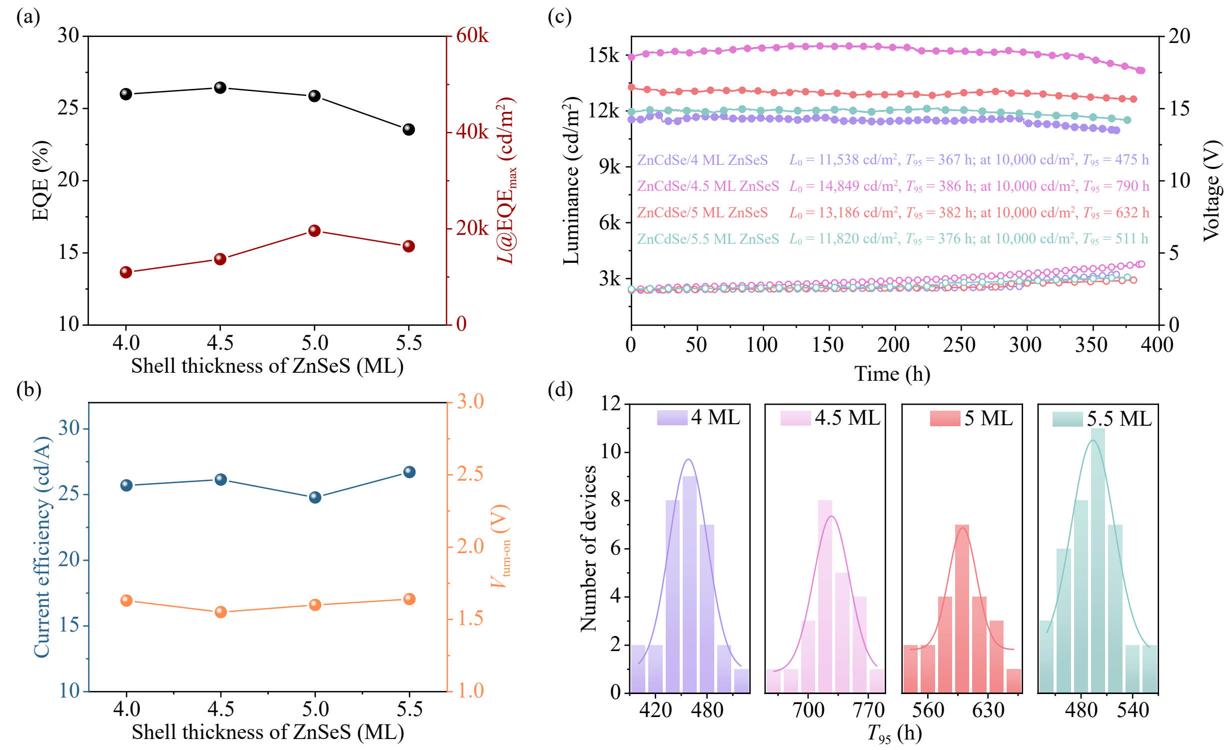

Figure 6 (a) EQE and luminance at the maximum EQE. (b) Current efficiency and $V_{\text{turn-on}}$. (c) L–time–V curves. (d) Histograms of T_{95} lifetimes with an initial luminance of 10,000 cd/m^2 from 31, 23, 23, and 39 devices using ZnCdSe QD-based devices with 4, 4.5, 5, and 5.5 ML ZnSeS shells.

interface. Shell composition tailoring leads to an increase in the upward band-bending and electron population, promoting charge injection balance and heat generation suppression. The synthesized ZnCdSe/ZnSeS QDs with further fine-tuning of the shell thickness could further effectively energy-band bending between the QD layer and HTL. Based on the shell-driven carrier engineering strategy, we achieved an EQE greater than 26% and a T_{95}@1000 cd/m^2 lifetime exceeding 50,000 h. Our work has provided a new strategy for effectively suppressing heat generation and has laid a material system for the commercialization of QLEDs.

Acknowledgements

The authors gratefully acknowledge the financial support from the National Natural Science Foundation of China (Nos. U22A2072, 22205054, and 61922028), the National Key Research and Development Program of China (No. 2023YFE0205000), Zhongyuan High Level Talents Special Support Plan (No. 244200510009), Key Research and Development and Promotion Project of Henan Province (Science and Technology Tackling Key Problems, No. 222102210271), and Postdoctoral Research Grant in Henan Province (No. 202103041).

Electronic Supplementary Material: Supplementary material (materials, preparation of Zn(OA)$_2$ precursor, synthesis of large-sized QDs, device fabrication, characterizations, schematic diagram of the QD synthesis, absorption and PL spectra, TEM images, XRD patterns, photoluminescence quantum yields (PLQYs), EL spectra, EQE–voltage curves, T_{95} lifetime measurements at different initial luminance, UPS spectra, J–L–V curves, and EQE–L–current efficiency curves) is available in the online version of this article at https://doi.org/10.1007/s12274-024-6899-4.

References

[1] Colvin, V. L.; Schlamp, M. C.; Alivisatos, A. P. Light-emitting diodes made from cadmium selenide nanocrystals and a semiconducting polymer. *Nature* **1994**, *370*, 354–357.

[2] Wu, Q. Q.; Gong, X. W.; Zhao, D. W.; Zhao, Y. B.; Cao, F.; Wang, H. R.; Wang, S.; Zhang, J. H.; Quintero-Bermudez, R.; Sargent, E. H. et al. Efficient tandem quantum-dot LEDs enabled by an inorganic semiconductor–metal–dielectric interconnecting layer stack. *Adv. Mater.* **2022**, *34*, 2108150.

[3] Shen, H. B.; Gao, Q.; Zhang, Y. B.; Lin, Y.; Lin, Q. L.; Li, Z. H.; Chen, L.; Zeng, Z. P.; Li, X. G.; Jia, Y. et al. Visible quantum dot light-emitting diodes with simultaneous high brightness and efficiency. *Nat. Photonics* **2019**, *13*, 192–197.

[4] Xu, H. Y.; Song, J. J.; Zhou, P. H.; Song, Y.; Xu, J.; Shen, H. B.; Fang, S. C.; Gao, Y.; Zuo, Z. J.; Pina, J. M. et al. Dipole–dipole-interaction-assisted self-assembly of quantum dots for highly efficient light-emitting diodes. *Nat. Photonics* **2024**, *18*, 186–191.

[5] Wang, Y.K.; Wan, H. Y.; Teale, S.; Grater, L.; Zhao, F.; Zhang, Z. D.; Duan, H. W.; Imran, M.; Wang, S. D.; Hoogland, S. et al. Long-range order enabled stability in quantum dot light-emitting diodes. *Nature* **2024**, *629*, 586–591.

[6] Cheng, Y.; Gui, Z. X.; Qiao, R. X.; Fang, S. C.; Ba, G. H.; Liang, T. Y.; Wan, H. Y.; Zhang, Z. H.; Liu, C.; Ma, C. J. et al. Electronic structural insight into high-performance quantum dot light-emitting diodes. *Adv. Funct. Mater.* **2022**, *32*, 2207974.

[7] Cao, W. R.; Xiang, C. Y.; Yang, Y. X.; Chen, Q.; Chen, L. W.; Yan, X. L.; Qian, L. Highly stable QLEDs with improved hole injection via quantum dot structure tailoring. *Nat. Commun.* **2018**, *9*, 2608.

[8] Deng, Y. Z.; Peng, F.; Lu, Y.; Zhu, X. T.; Jin, W. X.; Qiu, J.; Dong, J. W.; Hao, Y. L.; Di, D. W.; Gao, Y. et al. Solution-processed green and blue quantum-dot light-emitting diodes with eliminated charge leakage. *Nat. Photonics* **2022**, *16*, 505–511.

[9] Li, Z. H.; Chen, F.; Wang, L.; Shen, H. B.; Guo, L. J.; Kuang, Y. M.; Wang, H. Z.; Li, N.; Li, L. S. Synthesis and evaluation of ideal core/shell quantum dots with precisely controlled shell growth: Nonblinking, single photoluminescence decay channel, and suppressed FRET. *Chem. Mater.* **2018**, *30*, 3668–3676.

[10] Gao, Y.; Li, B.; Liu, X. N.; Shen, H. B.; Song, Y.; Song, J. J.; Yan, Z. J.; Yan, X. H.; Chong, Y. H.; Yao, R. Y. et al. Minimizing heat generation in quantum dot light-emitting diodes by increasing quasi-Fermi-level splitting. *Nat. Nanotechnol.* **2023**, *18*, 1168–1174.

[11] Lim, J.; Jeong, B. G.; Park, M.; Kim, J. K.; Pietryga, J. M.; Park, Y. S.; Klimov, V. I.; Lee, C.; Lee, D. C.; Bae, W. K. Influence of shell thickness on the performance of light-emitting devices based on CdSe/$Zn_{1-x}Cd_xS$ core/shell heterostructured quantum dots. *Adv. Mater.* **2014**, *26*, 8034–8040.

[12] Azadinia, M.; Chun, P.; Lyu, Q.; Cotella, G.; Aziz, H. Differences in electron and hole injection and auger recombination between red, green, and blue CdSe-based quantum dot light emitting devices. *ACS Nano* **2024**, *18*, 1485–1495.

[13] Acharya, K. P.; Nguyen, H. M.; Paulite, M.; Piryatinski, A.; Zhang, J.; Casson, J. L.; Xu, H. W.; Htoon, H.; Hollingsworth, J. A. elucidation of two giants: Challenges to thick-shell synthesis in CdSe/ZnSe and ZnSe/CdS core/shell quantum dots. *J. Am. Chem. Soc.* **2015**, *137*, 3755–3758.

[14] Yang, Y. X.; Zheng, Y.; Cao, W. R.; Titov, A.; Hyvonen, J.; Manders, J. R.; Xue, J. G.; Holloway, P. H.; Qian, L. High-efficiency light-emitting devices based on quantum dots with tailored nanostructures. *Nat. Photonics* **2015**, *9*, 259–266.

[15] Chen, D. S.; Chen, D.; Dai, X. L.; Zhang, Z. X.; Lin, J.; Deng, Y. Z.; Hao, Y. L.; Zhang, C.; Zhu, H. M.; Gao, F. et al. Shelf-stable quantum-dot light-emitting diodes with high operational performance. *Adv. Mater.* **2020**, *32*, 2006178.

[16] Dai, X. L.; Zhang, Z. X.; Jin, Y. Z.; Niu, Y.; Cao, H. J.; Liang, X. Y.; Chen, L. W.; Wang, J. P.; Peng, X. G. Solution-processed, high-performance light-emitting diodes based on quantum dots. *Nature* **2014**, *515*, 96–99.

[17] Lin, Q. L.; Wang, L.; Li, Z. H.; Shen, H. B.; Guo, L. J.; Kuang, Y. M.; Wang, H. Z.; Li, L. S. Nonblinking quantum-dot-based blue light-emitting diodes with high efficiency and a balanced charge-injection process. *ACS Photonics* **2018**, *5*, 939–946.

[18] Ji, W. Y.; Shen, H. B.; Zhang, H.; Kang, Z. H.; Zhang, H. Z. Over 800% efficiency enhancement of all-inorganic quantum-dot light emitting diodes with an ultrathin alumina passivating layer. *Nanoscale* **2018**, *10*, 11103–11109.

[19] Zhang, W. J.; Li, B.; Chang, C.; Chen, F.; Zhang, Q.; Lin, Q. L.; Wang, L.; Yan, J. H.; Wang, F. F.; Chong, Y. H. et al. Stable and efficient pure blue quantum-dot LEDs enabled by inserting an anti-oxidation layer. *Nat. Commun.* **2024**, *15*, 783.

[20] Kim, H. M.; Cho, S.; Kim, J.; Shin, H.; Jang, J. Li and Mg Co-doped zinc oxide electron transporting layer for highly efficient quantum dot light-emitting diodes. *ACS Appl. Mater. Interfaces* **2018**, *10*, 24028–24036.

[21] Jia, S. Q.; Hu, M. L.; Gu, M.; Ma, J. R.; Li, D. P.; Xiang, G. H.; Liu, P.; Wang, K.; Servati, P.; Ge, W. K. et al. Optimizing ZnO-quantum dot interface with thiol as ligand modification for high-performance quantum dot light-emitting diodes. *Small* **2024**, *20*, 2307298.

[22] Wang, Y. P.; Yang, Y. S.; Zhang, D. K.; Zhang, T.; Xie, S. Y.; Zhang, Y.; Zhao, Y. B.; Mi, X. Y.; Liu, X. L. Phosphorescent-dye-sensitized quantum-dot light-emitting diodes with 37% external quantum efficiency. *Adv. Mater.* **2023**, *35*, 2306703.

[23] Rhee, S.; Chang, J. H.; Hahm, D.; Jeong, B. G.; Kim, J.; Lee, H.; Lim, J.; Hwang, E.; Kwak, J.; Bae, W. K. Tailoring the electronic landscape of quantum dot light-emitting diodes for high brightness and stable operation. *ACS Nano* **2020**, *14*, 17496–17504.

[24] Li, Y.; Zhao, D. J.; Huang, W.; Jiao, Z. Q.; Wang, L.; Huang, Q. Y.; Wang, P.; Sun, M. N.; Yuan, G. C. Highly efficient quantum dot light-emitting diodes with the utilization of an organic emission layer. *Nano Res.* **2023**, *16*, 10545–10551.

[25] Song, J. J.; Wang, O. Y.; Shen, H. B.; Lin, Q. L.; Li, Z. H.; Wang, L.; Zhang, X. T.; Li, L. S. Over 30% external quantum efficiency light-emitting diodes by engineering quantum dot-assisted energy level match for hole transport layer. *Adv. Funct. Mater.* **2019**, *29*, 1808377.

[26] Yu, R. M.; Yin, F. R.; Zhou, D. W.; Zhu, H. B.; Ji, W. Y. Efficient quantum-dot light-emitting diodes enabled via a charge manipulating structure. *J. Phys. Chem. Lett.* **2023**, *14*, 4548–4553.

[27] Xu, M. P.; Chen, D. S.; Lin, J.; Lu, X. Y.; Deng, Y. Z.; He, S. Y.; Zhu, X. T.; Jin, W. X.; Jin, Y. Z. Quantum-dot light-emitting diodes with Fermi-level pinning at the hole-injection/hole-transporting interfaces. *Nano Res.* **2022**, *15*, 7453–7459.

[28] Lim, J.; Park, Y. S.; Wu, K. F.; Yun, H. J.; Klimov, V. I. Droop-free colloidal quantum dot light-emitting diodes. *Nano Lett.* **2018**, *18*, 6645–6653.

[29] Qu, X. W.; Ma, J. R.; Liu, P.; Wang, K.; Sun, X. W. On the voltage sweep behavior of quantum dot light-emitting diode. *Nano Res.* **2023**, *16*, 5511–5516.

[30] Zhang, H. M.; Wang, F. F.; Kuang, Y. M.; Li, Z. H.; Lin, Q. L.; Shen, H. B.; Wang, H. Z.; Guo, L. J.; Li, L. S. Se/S ratio-dependent properties and application of gradient-alloyed $CdSe_{1-x}S_x$ quantum dots: Shell-free structure, non-blinking photoluminescence with single-exponential decay, and efficient QLEDs. *ACS Appl. Mater. Interfaces* **2019**, *11*, 6238–6247.

[31] Ali Deeb, M.; Ledig, J.; Wei, J. D.; Wang, X.; Wehmann, H. H.; Waag, A. Photo-assisted Kelvin probe force microscopy investigation of three dimensional GaN structures with various crystal facets, doping types, and wavelengths of illumination. *J. Appl. Phys.* **2017**, *122*, 085307.

[32] Sun, X. X.; Wang, X. Q.; Liu, S. T.; Wang, P.; Wang, D.; Zheng, X. T.; Sang, L. W.; Sumiya, M.; Ueda, S.; Li, M. et al. Determination of the transition point from electron accumulation to depletion at the surface of $In_xGa_{1-x}N$ films. *Appl. Phys Express* **2018**, *11*, 021001.

[33] Bonilla, R. S. Modelling of Kelvin probe surface voltage and photovoltage in dielectric-semiconductor interfaces. *Mater. Res. Express* **2022**, *9*, 085901.

[34] Bodrozic, V.; Brown, T. M.; Mian, S.; Caruana, D.; Roberts, M.; Phillips, N.; Halls, J. J.; Grizzi, I.; Burroughes, J. H.; Cacialli, F. The built-in potential in blue polyfluorene-based light-emitting diodes. *Adv. Mater.* **2008**, *20*, 2410–2415.

[35] Lee, T.; Kim, B. J.; Lee, H.; Hahm, D.; Bae, W. K.; Lim, J.; Kwak, J. Bright and stable quantum dot light-emitting diodes. *Adv. Mater.* **2022**, *34*, 2106276.

[36] Zhang, H.; Su, Q.; Chen, S. M. Suppressing Förster resonance energy transfer in close-packed quantum-dot thin film: Toward efficient quantum-dot light-emitting diodes with external quantum efficiency over 21.6%. *Adv. Opt. Mater.* **2020**, *8*, 1902092.